OPEN ACCESS
IOP Publishing
Modelling and Simulation in Materials Science and Engineering
Modelling Simul. Mater. Sci. Eng. **32** (2024) 045011 (23pp) https://doi.org/10.1088/1361-651X/ad38d1

Phase-field modeling of stored-energy-driven grain growth with intra-granular variation in dislocation density

Guanglong Huang[1], Alexander Mensah[1], Marcel Chlupsa[1], Zachary Croft[2], Liang Qi[1], Ashwin J Shahani[1] and Katsuyo Thornton[1,*]

[1] Department of Materials Science and Engineering, University of Michigan, Ann Arbor, MI 48109, United States of America
[2] Applied Physics Program, University of Michigan, Ann Arbor, MI 48109, United States of America

E-mail: kthorn@umich.edu

Received 21 January 2024; revised 20 March 2024
Accepted for publication 28 March 2024
Published 16 April 2024

Abstract

We present a phase-field (PF) model to simulate the microstructure evolution occurring in polycrystalline materials with a variation in the intra-granular dislocation density. The model accounts for two mechanisms that lead to the grain boundary migration: the driving force due to capillarity and that due to the stored energy arising from a spatially varying dislocation density. In addition to the order parameters that distinguish regions occupied by different grains, we introduce dislocation density fields that describe spatial variation of the dislocation density. We assume that the dislocation density decays as a function of the distance the grain boundary has migrated. To demonstrate and parameterize the model, we simulate microstructure evolution in two dimensions, for which the initial microstructure is based on real-time experimental data. Additionally, we applied the model to study the effect of a cyclic heat treatment (CHT) on the microstructure evolution. Specifically, we simulated stored-energy-driven grain growth during three thermal cycles, as well as grain growth without stored energy that serves as a baseline for comparison. We showed that the

* Author to whom any correspondence should be addressed.

microstructure evolution proceeded much faster when the stored energy was considered. A non-self-similar evolution was observed in this case, while a nearly self-similar evolution was found when the microstructure evolution is driven solely by capillarity. These results suggest a possible mechanism for the initiation of abnormal grain growth during CHT. Finally, we demonstrate an integrated experimental-computational workflow that utilizes the experimental measurements to inform the PF model and its parameterization, which provides a foundation for the development of future simulation tools capable of quantitative prediction of microstructure evolution during non-isothermal heat treatment.

Supplementary material for this article is available online

Keywords: phase-field model, stored-energy-driven grain growth, dislocation density, cyclic heat treatment

1. Introduction

Polycrystalline materials are composed of an ensemble of grains with different crystallographic orientations, separated by grain boundaries. Since these boundaries possess excess energy, their reduction drives larger grains to grow and smaller grains to contract and eventually disappear during annealing. This phenomenon is referred to as *normal grain growth* (NGG). In NGG, after sufficient evolution, a self-similar state can be reached in which the scaled distribution of grain sizes remains unchanged [1, 2]. In some situations, however, a few grains grow exceptionally faster than others, leading to a non-self-similar grain-size distribution (GSD) [1, 3]. This phenomenon is referred to as *abnormal grain growth* (AGG). While AGG can be detrimental to materials properties in some situations [4, 5], it has been found to be useful in some applications, such as the fabrication of large-grained Fe–Si electrical steels with low core loss [6] and superior magnetic properties [7], and the production of Fe-based shape memory alloys with superior pseudoelastic properties [8]. Therefore, many studies have been conducted to identify its origin. For example, AGG was reported to occur within materials with a strong texture component [9–11] developed during recrystallization. Due to the presence of such texture, most of the grain boundaries have a low misorientation and thus possess a low grain boundary energy, leading to a small driving force for grain boundary migration to occur between these grains [1]. A few grains, however, may contain a different texture, which results in high-energy grain boundaries. These boundaries tend to migrate much faster than the other ones, leading to AGG [1]. Additionally, in two-phase systems, the second-phase particles are proposed to exert a pinning pressure on the grains in the matrix phase [12]. As a result, when the average grain size reaches a certain limit, which depends on the number and size of the second-phase particles, only those grains that are significantly larger than the average grain size can grow [2], resulting in the phenomenon of AGG.

In addition to the theories mentioned above, Omori *et al* [13] proposed that the subgrain structures formed within the preexisting grains in the process of cyclic heat treatment (CHT) play an important role in driving AGG. They first annealed a shape memory alloy of composition $Cu_{71.6}Al_{17}Mn_{11.4}$ at a high temperature (at which only body-centered-cubic (BCC) β phase exists at equilibrium) and then repeatedly cooled and heated the sample to below and above the face-centered-cubic (FCC) α solvus temperature, during which they observed AGG. Kusama *et al* [14] further developed the annealing schedule and showed that large single crystals can be produced under multiple cycles of the heat treatment. Omori *et al* [13] postulated

that the recurrent precipitation and dissolution of α phases within the β matrix during the non-isothermal annealing resulted in the loss of coherency of α–β interfaces, leading to the generation of dislocations within the sample. Consequently, subgrain structures form, which remain after precipitates dissolve. Omori *et al* [15] and Kusama *et al* [14] calculated the energy of subgrain boundaries to estimate the additional driving force for AGG upon CHT.

Higgins *et al* [16] interpreted this additional energy as the strain energy stored as dislocations, a common term that describes the driving force for recrystallization [17]. They postulated that the stored energy introduced within the grains *via* the formation of dislocations during the process of non-isothermal annealing would give rise to a driving force for the grains with lower stored energy to consume grains with higher stored energy, leading to the reduction of the total energy. They justified their hypothesis by performing real-time x-ray imaging experiments during CHT and showing that the grains in a Cu–Al–Mn sample with high dislocation density were consumed by those with low dislocation density. After ruling out the effects from texture and particle pinning, they proposed the stored energy due to the presence of dislocation is the primary mechanism for AGG during CHT of the Cu–Al–Mn alloy. Since the stored energy implicitly accounts for the energy associated with subgrain boundaries, as well as the lack thereof in the low-misorientation regions where subgrains are not identified, it provides a more general measure of the driving force relevant to CHT. We follow this approach herein to further evaluate the effect of this additional driving force on grain growth microstructures.

To work in concert with the experimental characterization tools to provide an in-depth understanding of how the combined effects of grain boundary energy and the stored energy impact the microstructure evolution within a sample undergoing CHT, a computational model that considers both driving forces is necessary. Phase-field (PF) models are commonly utilized to simulate microstructure evolution [18–20], such as solidification [21–24], recrystallization [25, 26], and chemical reaction [27–29]. In a PF model, the thermodynamics for the material system being modeled is incorporated into the free energy functional that is used to compute the driving force for evolution, and the microstructure is described by field variables (often referred to as order parameters) that can be conserved or non-conserved over the domain. For the study of grain growth [30–32], order parameters are employed to indicate the volume occupied by individual grains as well as the boundaries between these grains. A few PF models have been developed to study the influence of anisotropy in grain boundary energy [33], anisotropy in grain boundary mobility [34, 35], and second-phase particles [36] on the dynamics of AGG. Higgins *et al* presented a PF model [16] that extended recrystallization models developed by Moelans *et al* [37] and Gentry and Thornton [25] to account for the contribution of stored energy as the driving force for grain boundary migration. Their simulations showed that the additional driving force allows for the grains with a low dislocation density to consume the grains with a high dislocation density. This model assumes that each grain possesses a spatially uniform dislocation density, and that the region traversed by a grain boundary inherits the dislocation density value of the grain that grows into this region. However, recent imaging experiments (detailed in section 2) suggest that the dislocation density is inhomogeneous even within an individual grain and that the traversed region appears to have a reduced dislocation density, resulting in a variation in the intra-granular dislocation density. In order to capture the effects of these features on microstructure evolution undergoing CHT, it is necessary to extend the PF model presented by Higgins *et al* [16].

In this work, we introduce a PF model to simulate the evolution of microstructure with variation in the intra-granular dislocation density and show how synchrotron high-energy x-ray diffraction microscopy (HEDM) data of a sample undergoing CHT can inform this model.

We first demonstrate that the proposed PF model yields results that closely resemble the experimental data, and then we apply the model to simulate the microstructure evolution on a larger scale to examine the effect of CHT.

2. Real-time experimental study of microstructure evolution in Cu–Al–Mn

We performed a single cycle of heat treatment on a cylindrical $Cu_{71.6}Al_{17}Mn_{11.4}$ alloy, following the protocol given in [13, 14]. HEDM experiments were conducted on this material at the 1-ID beamline of the Advanced Photon Source at Argonne National Laboratory, using a new infrared furnace described in [16]. The cylindrical samples were vertically mounted on the rotation stage and rotated about an axis parallel to gravity, which is orthogonal to the plane defined by the line focused beam. In a near-field geometry [38], the detector captured 720 diffraction images (0.25° intervals spanning 180°) for each quasi-two-dimensional (2D) 'slice' of the sample, where slices were separated by 7 μm in the first two states and 14 μm in the third, along the axis of rotation. Data were collected at sample-to-detector distances of 10 mm and 12 mm. The schedule for dynamic annealing is shown in figure 1.

The first acquisition (S_1) was performed at room temperature on a fully recrystallized sample of the BCC-β phase, before any annealing was conducted to promote grain growth. Diffraction patterns from *in-situ* far-field HEDM were used to monitor the microstructure evolution upon annealing in real time, such that the sample was air quenched when the FCC-α (second-phase particles) spot intensities stopped increasing. The second acquisition (S_2) was performed on this particle-rich state. The annealing process then resumed with a fast ramp up to the previous temperature followed by a slower ramp toward and exceeding the FCC-α solvus temperature. After the FCC-α rings disappeared in the far-field HEDM images, the sample was air quenched. The third acquisition (S_3) was performed on the particle-depleted state. The set of three acquisitions ($S_1 \rightarrow S_2 \rightarrow S_3$) represents one cycle of heat treatment. After the experiment, the diffraction images were reconstructed in 2D *via* the forward model [39, 40] based HEXOMAP [16] and analyzed *via* PolyProc [41].

To demonstrate the integrated experimental-computational workflow, we utilize the reconstructed microstructure and dislocation density obtained in the experiments to inform our PF model. While the simulation should ideally be done in three dimensions, in this work, we chose to conduct 2D simulations, which are computationally efficient and sufficient for demonstrating the integrated workflow. Even though matching the experimental and computational results is not our primary focus, we find that simulation predictions agree qualitatively with the experimentally observed evolution, as we discuss later.

We employ the grain and dislocation density maps within a 2D slice of the sample at states S_1 and S_2, as shown in figure 2. This particular slice is selected since it includes an apparently confined region (i.e. the outer boundaries of this region are nearly static throughout the experiment). By considering this confined region, which consists of several grains in the S_1 state, indicated by a black contour in figure 2(a) (S_1) and (b) (S_2), we reduce the cost of the simulations while allowing for a comparison between experiments and simulations. Additionally, it appears that only few new grains emerge from state S_1 to S_2 (by comparing figures 2(a) and (b)), indicating that the microstructure evolution along the dimension perpendicular to the slice plane does not greatly influence the microstructure evolution within this slice. By comparing figures 2(c) and (d), it is also clear that the grain G_1 is consuming the surrounding grains and is the only grain that remains at state S_2. The dislocation density of the confined region at S_1 (see figure 2(e)) is relatively uniform, which is expected since the sample has not yet been dynamically annealed. As the sample is progressively heated from S_1 to S_2, the

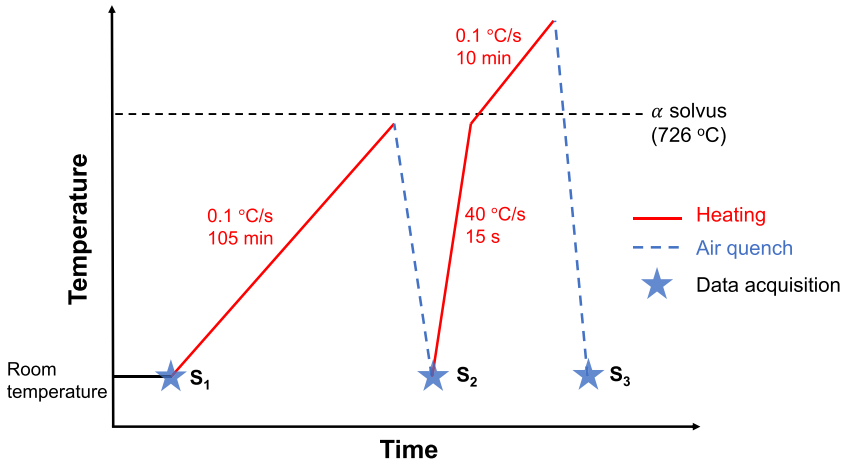

Figure 1. Schematic of dynamic annealing schedule in the interrupted *in-situ* HEDM experiment. The axes are not to scale. The data acquisitions are indicated by blue star; the red solid lines indicate heating, while the blue dash lines indicate cooling. The α-solvus temperature is indicated by the black dash line.

dislocations are formed within each grain with a different density, which could be attributed to the difference in the density of second-phase particles precipitated during annealing [16]. As noted previously, differences in dislocation density provide a driving force for the grains with a lower dislocation density to consume those grains with a higher dislocation density. Figure 2(f) shows the dislocation density of the confined region at state S_2. It can be observed that the dislocation density is higher within the region initially occupied by G_1, as compared to the surrounding area, which suggests that the dislocation density in the region traversed by the grain boundary is reduced.

To examine the effect of CHT on the microstructure evolution, it is necessary to track the change of the GSD over time, which requires a sufficiently large number of grains for meaningful statistics throughout the simulation. Since state S_1 contains a large number of grains and corresponds to the starting point of the heat treatment cycle in the experiment, we use the GSD in state S_1 (evaluated from the entire volume; see figure 3(a)) to initialize a microstructure for the large-scale simulations. Likewise, the GSDs for states S_2 and S_3 are shown in figures 3(b) and (c), respectively. Given the fact that the average grain radius for the entire three-dimensional (3D) volume increases by $\sim$40% from state S_1 to S_3 in the experiment, we set this percentage of increase in the average grain radius as the stopping criteria in our simulation of one heat treatment cycle.

3. Methods

3.1. Individual dislocation density field

To account for the variation in intra-granular dislocation densities observed in the HEDM experiments, we introduce an *individual dislocation density field*, ρ_i, for each grain i, which stores not only the initial dislocation density value for that grain but also what the dislocation density value would be if the grain boundary of the grain were to reach that position. While the

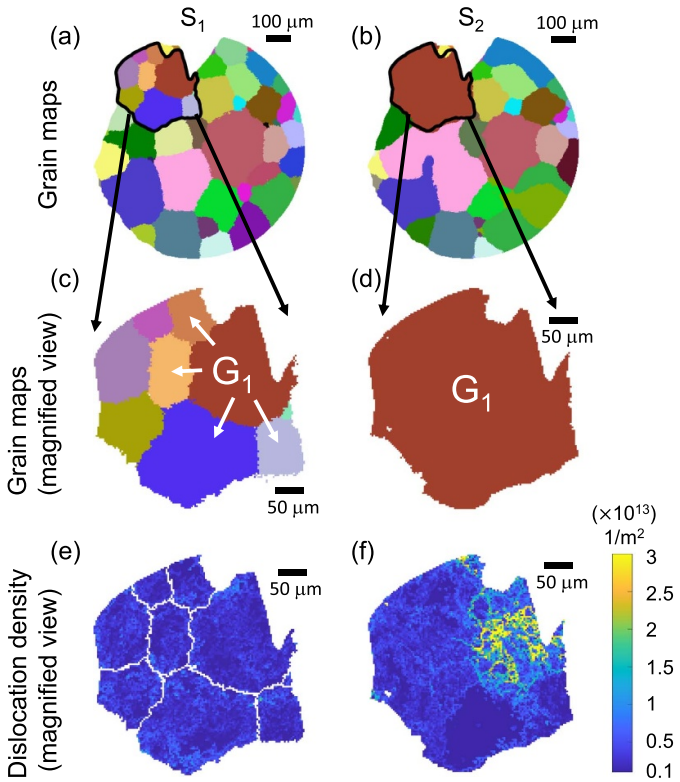

Figure 2. Grain and dislocation density maps for a selected cross-sectional slice of the cylindrical sample, measured at state S_1 (left column) and S_2 (right column). (a), (b) Grain maps at state S_1 and S_2, respectively. An apparently confined region is indicated by a black contour. Each grain is indicated by a unique, random color. The same color is assigned to the same grain appearing in both states. (c), (d) Magnified view of the grain map for the confined region at state S_1 and S_2, respectively. Grain G_1 consumes the surrounding grains from state S_1 to S_2, respectively. (e), (f) Dislocation density field within the confined region at state S_1 and S_2, respectively.

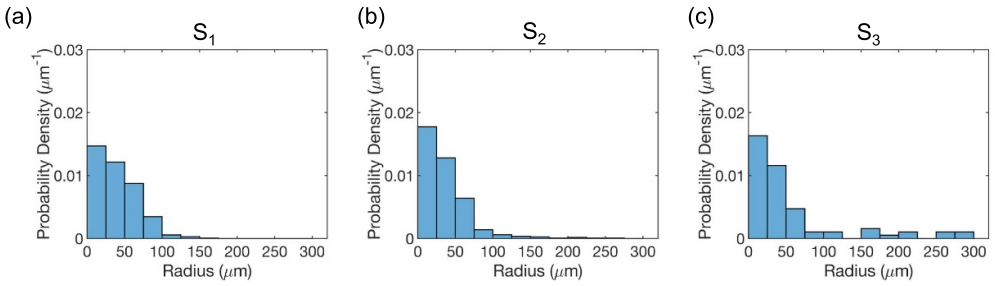

Figure 3. Grain size distribution for the entire volume of (a) state S_1, (b) state S_2, and (c) state S_3 determined from the HEDM data. The grain size is evaluated as the equivalent radius, assuming a circular shape of the grain.

exact mechanism by which the reduction in the dislocation density occurs has yet to be investigated, there are multiple mechanisms that would lead to an elimination of dislocations as a grain boundary migrates, including annihilation of dislocation pairs and absorption of dislocations onto grain boundaries [42, 43]. The enhancement of the rate by which these processes occur (vs. recovery in the bulk, which appears to be slow on the time scale of the experiment) is expected from the fact that grain boundary migration requires atomic rearrangements and consequently changes the strain fields. Below, we derive a model for dislocation density evolution that accounts for such a process, which is used to define ρ_i.

Mathematically, it is reasonable to assume that the dislocation density is reduced at a rate, $\frac{\mathrm{d}\rho}{\mathrm{d}x}$, that is proportional to how many dislocations per unit volume exist at the grain boundary position as the grain boundary migrates:

$$\frac{\mathrm{d}\rho}{\mathrm{d}x} = -\frac{\rho}{l_e}, \tag{1}$$

where x is the distance traversed by the grain boundary and the inverse of l_e provides the rate constant for the decay. This differential equation can be solved analytically, yielding

$$\rho = \rho_{\mathrm{gb}} \exp\left(-\frac{x}{l_e}\right), \tag{2}$$

where ρ_{gb} is the dislocation density just behind the initial grain boundary and the constant l_e can now be identified as the length scale at which the dislocation density decays by a factor of e in the wake of the migrating grain boundary. We assume that grain boundaries migrate in their normal direction, which is a simplifying assumption, and therefore the value of x can be determined from a signed distance function using the level-set method (detailed in section S1 of the supplementary material).

We now describe how this model is implemented. As in figure 2, we denote the grain with index i as G_i. For each grain G_i, we employ a time- and position-dependent order parameter field $\eta_i(\boldsymbol{r}, t)$ to track its evolution. The value of $\eta_i(\boldsymbol{r}, t)$ is 1 within the grain, 0 outside the grain, and varies smoothly from 1 to 0 across its interface. In this work, we omit the effect of recovery, and therefore the dislocation density at a certain position, r, retains its initial value until the grain boundary from another grain reaches this point, at which time a reduced dislocation density is assigned, according to equation (2). Since we do not allow dislocation density to evolve otherwise, this model introduces discontinuities in the gradient of dislocation density, which persist; if we consider recovery, the magnitude of such discontinuities would gradually reduce and eventually vanish. We precompute the reduced dislocation density for each grain in regions not initially occupied by the grain and store these values into its individual dislocation density field $\rho_i(\boldsymbol{r})$, along with its initial dislocation density values within the grain. Specifically, ρ_i is defined as

$$\rho_i(\boldsymbol{r}) = \begin{cases} \rho_{0,i}(\boldsymbol{r}), & \text{within Grain } G_i \\ \max\left(\rho_{\mathrm{base}}, \rho_{\mathrm{gb,i}} \exp\left(-\frac{|d_i(\boldsymbol{r})|}{l_e}\right)\right), & \text{otherwise} \end{cases}. \tag{3}$$

Here, $\rho_{0,i}(\boldsymbol{r})$ is the initial dislocation density within grain G_i, $\rho_{\mathrm{gb},i}$ is the dislocation density just behind G_i's initial boundary, and $d_i(\boldsymbol{r})$ is the signed distance between the point r and the nearest point to the G_i's initial boundary; note that the sign of $d_i(\boldsymbol{r})$ is taken to be positive within the grain and negative outside, and therefore $d_i(\boldsymbol{r}) < 0$ in equation (3). The term ρ_{base} in equation (3) denotes a *baseline dislocation density, i.e.,* the lower bound for the dislocation density measured in the experiment, that remains even after a long period of annealing.

In general, $\rho_{\mathrm{gb},i}$ is a spatially varying quantity, but we here assume it to be a constant for each grain, as discussed in section 3.4.2. We found that simulations with $l_e = 20$ μm yield results that closely resemble the experimental observations, and thus we employ this value throughout this work. We estimate the baseline dislocation density ρ_{base} to be 3×10^{12} m^{-2} by taking the average of the dislocation densities at state S_2 for the regions outside grain G_1's initial position (indicated in figure 2(c)). While this may slightly overestimate the base value because it may include some enhanced dislocation density near the initial grain boundaries, we deemed this assumption to be reasonable given the statistical variation and uncertainties in the measurements [44]. In addition, the determined value of ρ_{base} is of the same order of magnitude as dislocation densities in well-annealed metals (2×10^{11} m^{-2} to 3×10^{12} m^{-2} [45]), which supports the validity of the assumption. Further details are provided in section 3.4.2.

It is necessary to note that the values of $\rho_i(\boldsymbol{r})$ outside the boundaries of the initial grains should not be considered as physical values, other than the fact that it sets the value of the dislocation density if the grain boundary of G_i sweeps past the point. Rather, at any point in time, the actual dislocation density is given by constructing it from $\{\rho_i(\boldsymbol{r})\}$, along with the set of order parameters $\{\eta_i(\boldsymbol{r},\ t)\}$, using the following interpolation function:

$$\rho(\boldsymbol{r},t) = \frac{\sum_{i=1}^{N} \eta_i^2(\boldsymbol{r},t)\,\rho_i(\boldsymbol{r})}{\sum_{i=1}^{N} \eta_i^2(\boldsymbol{r},t)}. \tag{4}$$

This formula is identical to those used in [16, 25, 37, 46], except that in these previous works, ρ_i was a constant associated with the i^{th} grain, and therefore these models could not treat intra-granular inhomogeneity nor a decay in the dislocation density as the grain boundaries migrate.

To facilitate our understanding of dislocation density evolution based on the above formulation, we provide schematics in figure 4 showing the change in the dislocation density field as grain G_i consumes its surrounding grains. The grains that are adjacent to G_i are omitted in figure 4(a) for clarity. Grain G_i, indicated in blue, initially possesses dislocation density $\rho_{\mathrm{gb},i}$ at the position of its grain boundaries. As it progressively consumes its surrounding grains with higher dislocation density (denoted by ρ_{surr} in figure 4) and reaches the point A at time t_1, the dislocation density reduces to a value given by $\rho_{\mathrm{gb},i}\exp\left(-\frac{|d_i(A)|}{l_e}\right)$. As the grain continues to grow to point B at time t_2, where by $\rho_{\mathrm{gb},i}\exp\left(-\frac{|d_i(B)|}{l_e}\right) = \rho_{\mathrm{base}}$, the dislocation density value behind the migrating grain boundary reduces to the baseline dislocation density ρ_{base}, which is the lower bound of the dislocation density. Beyond this point, the dislocation density behind the grain boundary remains at ρ_{base}; for example, when the grain boundary reaches point C at time t_3, the dislocation density at point C reduces to ρ_{base}.

3.2. PF equations

A total free energy functional that encodes the thermodynamics of the polycrystalline material is given by the volume integral of the sum of three energy density terms:

$$\mathcal{F}(\{\eta_i\}) = \int_V \left(f_{\mathrm{bulk}} + f_{\mathrm{gradient}} + f_{\mathrm{stored}}\right) \mathrm{d}V. \tag{5}$$

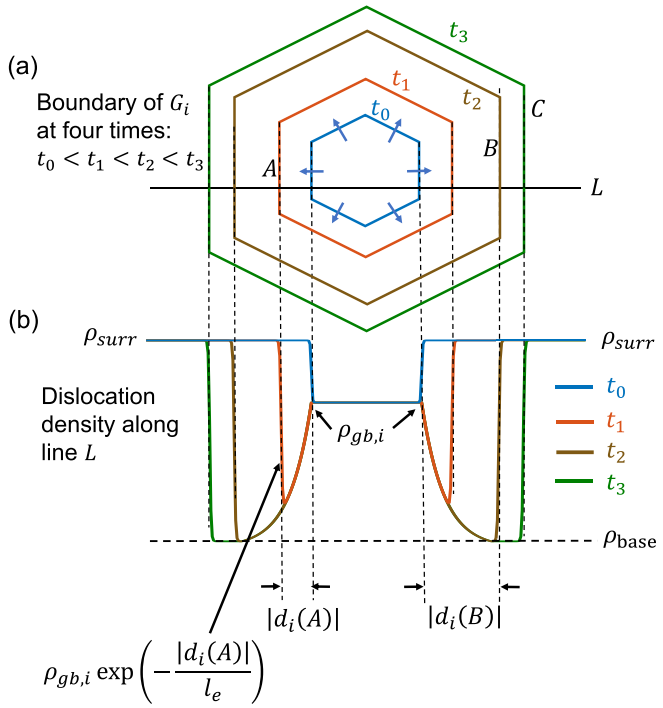

Figure 4. Schematics showing the evolution of a dislocation density field at four time-points when grain G_i consumes its surrounding grains, assuming an exponential decay of dislocation densities. For illustrative purposes, the first cycle is assumed. (a) Grain boundaries of G_i at four times, $t_0 < t_1 < t_2 < t_3$, which are indicated in blue, red, brown, and green, respectively. The grains that are adjacent to G_i are omitted for clarity. (b) The dislocation density field along the line L in (a) at the four times. The baseline dislocation density, dislocation density at the grain boundary, and dislocation density of the surrounding grains are denoted by ρ_{base}, $\rho_{\text{gb},i}$, and ρ_{surr}, respectively. Note that the signed distance $d_i < 0$ outside of the region initially occupied by the grain.

We utilize the functional form proposed by Moelans *et al* [47] to calculate the bulk energy density, f_{bulk}:

$$f_{\text{bulk}} = W\left[\sum_{i=1}^{N}\left(-\frac{1}{2}\eta_i^2 + \frac{1}{4}\eta_i^4\right) + \alpha\sum_{i=1}^{N}\sum_{j>1}^{N}\left(\eta_i^2\eta_j^2\right) + \frac{1}{4}\right], \tag{6}$$

where W is the bulk energy density coefficient, and $\alpha = 1.5$ is set to ensure a symmetrical order parameter profile across an interface, as discussed in [47]. The gradient energy density [20, 48], f_{gradient}, is employed to penalize a sharp interface,

$$f_{\text{gradient}} = \frac{\kappa}{2}\sum_{i=1}^{N}|\nabla\eta_i|^2, \tag{7}$$

where κ is the gradient energy coefficient. The values of W and κ are determined based on the grain boundary energy, γ_{gb}, a material parameter, and the grain boundary width, l_{gb}, a model parameter, using the formula derived by Moelans *et al* [47]:

$$W = \frac{6\gamma_{\mathrm{gb}}}{l_{\mathrm{gb}}}, \tag{8}$$

$$\kappa = \frac{3}{4}\gamma_{\mathrm{gb}} l_{\mathrm{gb}}. \tag{9}$$

The grain boundary energy for Cu–Zn [49], $\gamma_{\mathrm{gb}} \approx 0.595$ J m^{-2}, is employed here for Cu–Al–Mn, due to a lack of data on the latter system. An approximate form [17], which neglects the energy of the dislocation core and assumes isotropic elasticity, is utilized to describe the stored energy density, f_{stored}, due to the presence of the dislocation density, $\rho(\boldsymbol{r},t)$, as

$$f_{\mathrm{stored}} = \frac{1}{2} G b^2 \rho(\boldsymbol{r},t), \tag{10}$$

where $G = 28.4$ GPa is the shear modulus for the β phase of Cu–Al–Mn alloy at 650 °C, calculated by [14] based on [50]. The magnitude of the Burger's vector for the FCC copper [51], $b = 0.255$ nm, is used here as an estimate value for the copper-rich Cu–Al–Mn alloy. The evolution of the order parameter η_i is obtained via steepest descent, using Allen–Cahn dynamics [52]:

$$\frac{\partial \eta_i}{\partial t} = -L\left(\frac{\delta F}{\delta \eta_i}\right), \tag{11}$$

where L is the mobility parameter. Substituting equations (5)–(7) and (10) into equation (11) yields

$$\frac{\partial \eta_i}{\partial t} = -L\left[W\left(-\eta_i + \eta_i^3 + 2\alpha\eta_i \sum_{\substack{j=1 \\ j\neq i}}^{N} \eta_j^2\right) - \kappa\nabla^2\eta_i + Gb^2 \frac{\eta_i}{\sum_{j=1}^{N}\eta_j^2}\left(\rho_i(\boldsymbol{r}) - \rho\right)\right]. \tag{12}$$

3.3. Nondimensionalization of PF equations

We chose 40 μm as the length scale, which is on the order of the radius of a typical grain in our simulations. We divide all the lengths by l_0 to obtain their dimensionless forms. We select the bulk energy density coefficient W in equation (6) as the energy scale and divide all the energies by W to nondimensionalize them. We denote $\bar{\rho}_{\mathrm{init}}$ as the spatial average of $\rho(r, t=0)$ over the entire computational domain (excluding the non-solid region defined by the dummy order parameter in section 4.1) and utilize this value to scale $\{\rho_i(\boldsymbol{r})\}$ and $\rho(\boldsymbol{r},t)$. After these scaling quantities are chosen, we set the time scale to

$$t_0 = \frac{1}{WL}. \tag{13}$$

Table 1. Dimensional and dimensionless phase-field variables.

Variable	Nondimensionalized variable
W	$W^* = \frac{W}{W} = 1$
κ	$\kappa^* = \frac{\kappa}{WL_0^2} = \frac{1}{8}\left(\frac{l_{gb}}{l_0}\right)^2$
L	$L^* = \frac{L}{L} = 1$
$\boldsymbol{r}$	$\boldsymbol{r}^* = \frac{\boldsymbol{r}}{l_0}$
t	$t^* = \frac{t}{t_0} = WLt$
ρ_i	$\rho_i^* = \frac{\rho_i}{\bar{\rho}_{\text{init}}}$
ρ	$\rho^* = \frac{\rho}{\bar{\rho}_{\text{init}}}$

We divide the time by this scale, and rearrange the resulting equation, which results in the dimensionless form of equation (12). The dimensional and dimensionless quantities are summarized in table 1. The dimensionless quantities are denoted by their counterpart accompanied by an asterisk ($*$) in their superscripts. We employ the dimensionless quantities for the study, which can be converted into dimensional quantities based on the scaling factors.

3.4. Methods for setting up initial conditions

The initial condition for each simulation is composed of two parts: an initial microstructure described by a set of order parameters $\{\eta_i(\boldsymbol{r}, t=0)\}$, and a set of corresponding individual dislocation densities, $\{\rho_i(\boldsymbol{r})\}$. In this work, we perform two sets of 2D simulations. The first set of simulations directly imports a grain map from the experimental cross-sectional data containing a relatively small number of grains, while the second set of simulations leverages the GSD from the experimental data to initialize a synthetic microstructure that contains a large number of grains.

3.4.1. Initialization of order parameters. First, the microstructure at state S_1 captured in the experiment is processed to produce a set of binary fields $\{n_i(\boldsymbol{r})\}$. For the first set of simulations, the 2D grain map, $\Omega(\boldsymbol{r})$, of the confined region at S_1, which marks the region of each grain with a unique but consecutive integer, is used to initialize a set of $n_i(\boldsymbol{r})$ fields according to

$$n_i(\boldsymbol{r}) = \begin{cases} 1, & \text{if } \Omega(\boldsymbol{r}) = i \\ 0, & \text{otherwise} \end{cases}. \tag{14}$$

For the second set of simulations, the GSD calculated from the entire 3D volume of the sample at the S_1 state (figure 3(a)) is converted to a 2D GSD by implementing an established method in stereology [53, 54] in a reversed manner, as detailed in section S2 of the supplementary material. The 2D GSD is then used to inform the selection of the locations of K seeds of grains, as detailed in section S3 of the supplementary material. A set of binary fields $\{n_i(\boldsymbol{r})\}$ is then constructed from the locations of K seeds of grains, using the method discussed in section 3.5.

For both cases, the set of binary fields $\{n_i(\boldsymbol{r})\}$ is evolved via Allen–Cahn dynamics without the stored-energy for a dimensionless time of t^*_{ini}, just long enough to obtain the order parameters with diffuse interfaces, $\{\eta_i(\boldsymbol{r})\}$. The parameters employed for this smoothing process for the small- and large-scale simulations are summarized in tables 2 and 3, respectively. As mentioned earlier, the grain boundary energy for Cu–Zn [49], $\gamma_{gb} \approx 0.595$ J m^{-2}, is employed here for Cu–Al–Mn, which was consistent with Kusama's study [14]. For interfacial width,

Table 2. Parameters employed for the small-scale simulations to generate the order parameters from the binary fields. Dimensional values in parentheses denote numerical parameters (not physical parameters).

Parameters	Variable	Value (dimensionless)	Value (dimensional)
Grain boundary energy	γ_{gb}	1.67×10^{-2}	0.595 J m^{-2}
Grain boundary width	l_{gb}	0.1	(4 μm)
Domain size	l	12	4.80×10^{2} μm
Grid spacing	$\Delta x = \Delta y$	2.50×10^{-2}	(1 μm)
Bulk energy coefficient	W	1	Not applicable
Gradient energy coefficient	κ	1.25×10^{-3}	Not applicable
Time step size	Δt	0.1	Not available
Duration	t_{ini}	100	Not available

Table 3. Parameters employed for the large-scale simulations to generate the order parameters from the binary fields. Dimensional values in parentheses denote numerical parameters (not physical parameters).

Parameters	Variable	Value (dimensionless)	Value (dimensional)
Grain boundary energy	γ_{gb}	1.46×10^{-2}	0.595 J m^{-2}
Grain boundary width	l_{gb}	8.75×10^{-2}	(3.5 μm)
Domain size	l	69.43	2.78×10^{3} μm
Grid spacing	$\Delta x = \Delta y$	2.19×10^{-2}	(0.876 μm)
Bulk energy coefficient	W	1	Not applicable
Gradient energy coefficient	κ	9.57×10^{-4}	Not applicable
Time step size	Δt	0.1	Not available
Duration	t_{ini}	50	Not available

domain size, and grid spacing, both dimensionless and dimensional values are presented. Since bulk energy coefficient and gradient energy coefficient are model parameters that are calculated from the dimensionless values of grain boundary energy and grain boundary width, only dimensionless values of them are presented. The conversion of dimensionless time to dimensional time is complicated because it requires the mobility parameter L, which depends on the temperature and was not reported for Cu–Al–Mn alloy under a non-isothermal annealing condition. Thus, this study focuses on qualitative agreement between the dynamics observed in simulations and experiments. Note that the initial microstructure for the small-scale simulations is derived from the experimental measurement and contained tiny grains that cannot be resolved by the PF model. Therefore, it was necessary to apply the smoothing operation longer (about twice as long) until these grains are eliminated during the smoothing process. In addition, slight adjustments were needed in the grid spacing and related parameters due to the domain size change.

3.4.2. Construction of individual dislocation density fields. As seen in equation (3), the initial dislocation density $\rho_{0,i}(\boldsymbol{r})$ and the distance function $d_i(\boldsymbol{r})$ for each grain G_i are two required components to construct an individual dislocation density field $\rho_i(\boldsymbol{r})$. Although in reality a cycle of heat treatment involves continuous dislocation generation and microstructure evolution, we model this process by injecting all the generated dislocations, $\Delta\rho_i$, at the start of the thermal treatment cycle; thus, this term is added to the baseline value before the microstructure evolution is simulated. A more sophisticated approach that considers the dynamic generation

of dislocations during precipitation will be left for future work. Given the experimental observations that a majority of the second-phase particles is found on or near the grain boundaries and the fact that a small grain has a higher line length per unit area in two dimensions (equivalent to surface area per unit volume in three dimensions) than a large grain, we propose that the density of second-phase particles is higher in a small grain. Additionally, it is reported in [16] that the relationship between the grain-averaged dislocation density and the density of second-phase particles can be roughly described by a positive linear correlation. We therefore postulate that the value of $\Delta\rho_i$ is inversely proportional to the equivalent radius (assuming a circular shape), R_i, of grain G_i, according to

$$\Delta\rho_i = \frac{k_\rho}{R_i}. \tag{15}$$

The value of k_ρ is estimated by substituting the known values of $\Delta\rho_1$ and R_1 for grain G_1 within the confined region (see figure 2) into equation (15). To do so, $\Delta\rho_1$ is estimated by subtracting the baseline dislocation density from the average dislocation density of G_1 at S_2 within its initial position at S_1. The value of the equivalent radius R_1 is determined for G_1 based on its area at S_1. Accordingly, the value of k_ρ is found to be 8×10^8 m^{-1}.

When considering multiple cycles, each cycle must be initialized based on either the initial state of the sample or the state from the previous cycle. Hereafter in this section, we add the cycle number on the superscript of the dislocation density to indicate the cycle number. The individual dislocation density at positions initially within grain G_i for the first cycle, $\rho^1_{0,i}(\boldsymbol{r})$, is set by adding $\Delta\rho_i$ to the baseline dislocation density ρ_{base}:

$$\rho^1_{0,i}(\boldsymbol{r}) = \Delta\rho_i + \rho_{\text{base}} = \frac{8 \times 10^8 \text{ m}^{-1}}{R_i} + 3 \times 10^{12} \text{ m}^{-2}. \tag{16}$$

To set the individual dislocation density at positions initially outside of grain G_i, we first apply the level-set method discussed in section S1 of the supplementary material to obtain the distance function, $d_i(\boldsymbol{r})$, based on the order parameter $\eta_i(\boldsymbol{r})$. Since $\rho^1_{0,i}(\boldsymbol{r})$ is a constant for the first cycle, as indicated by equation (16) and illustrated in figure 4(b) (see the blue line), the individual dislocation density at the grain boundary, $\rho^1_{\text{gb},i}$, is equal to this constant value given by

$$\rho^1_{gb,i} = \Delta\rho_i + \rho_{\text{base}} = \frac{8 \times 10^8 \text{ m}^{-1}}{R_i} + 3 \times 10^{12} \text{ m}^{-2}. \tag{17}$$

Equation (3) is then employed to generate the individual dislocation density field $\rho^1_i(\boldsymbol{r})$ for the first cycle.

To reinject dislocations at the beginning of each subsequent cycle C $(C > 1)$, the value of the individual dislocation density at positions initially within G_i for the subsequent cycle, $\rho^C_{0,i}(\boldsymbol{r})$, is set by adding $\Delta\rho_i$ to its individual dislocation density at the end of the previous cycle, $\rho^{C-1}_{f,i}(\boldsymbol{r})$:

$$\rho^C_{0,i}(\boldsymbol{r}) = \Delta\rho_i + \rho^{C-1}_{f,i}(\boldsymbol{r}) = \frac{8 \times 10^8 \text{ m}^{-1}}{R_i} + \rho^{C-1}_{f,i}(\boldsymbol{r}). \tag{18}$$

We assume that after each cycle of grain growth, the value of dislocation density at the grain boundary of each remaining grain is reduced to a value that is sufficiently close to the baseline

dislocation density. Thus, for simplicity, the individual dislocation density at the grain boundary for the cycle C (where $C > 1$), $\rho^{C}_{\mathrm{gb},i}$, is set again using equation (17). Then, equation (3) is employed to generate the initial dislocation density field $\rho^{C}_{i}(\boldsymbol{r})$, where $C > 1$.

3.5. Assigning multiple grains to an order parameter

Although the implementation is simple when an order parameter is used to track one grain, the computation becomes expensive when the simulation involves a large number of grains, as in the second set of simulations. To enable large-scale simulation of microstructure evolution in an efficient manner, we require the capability to track multiple grains with one order parameter, which reduces the total number of order parameters required for the simulations. However, it is necessary to ensure that the grains tracked by the same order parameter do not overlap during the microstructure evolution to avoid grain coalescence (and, for our model, that the decaying individual dislocation density fields do not overlap, which would introduce numerical artifacts). The grain remapping schemes [32, 55, 56] have been proposed in the literature for PF simulations of grain growth, which reassign a grain to a different order parameter when the grain is too close to another grain tracked by the same order parameter. However, the standard remapping scheme cannot be applied without modifications because of the necessity to track the decay in the dislocation density outside of the grains. Therefore, we take a simpler approach in which grains are placed sufficiently far apart initially and are not dynamically remapped. In practice, we assign up to nine grains to one order parameter to reduce the number of required order parameters (and thus the number of equations to be evolved) and employ a corresponding individual dislocation density field to track the decay in dislocation densities for these grains. The detailed procedure is described in section S4 of the supplementary material.

4. Results and discussion

4.1. Microstructure evolution within a confined region

In this section, we apply the PF model to study the evolution of microstructure and dislocation density within a confined region observed in the experiment (see figures 2(c)–(f)), as discussed in section 2. We select 4 μm as the interfacial width, which is $\sim$1/10 of the radius of a typical grain in our simulations and is sufficient to resolve the grains in the confined region. The order parameters are initialized using the method discussed in section 3.4.1. Since the boundary of the confined region is not rectangular, we utilize a dummy order parameter, which is not evolved throughout the microstructure evolution, to describe the area surrounding the confined region. The individual dislocation densities are initialized using equation (3), with $\rho_{0,i}(\boldsymbol{r})$ given by equation (16) and $\rho_{\mathrm{gb},i}$ given by equation (17). The dimensionless parameters employed for the simulation are summarized in table 4.

The initial microstructure is shown in figure 5(a). Each grain is assigned to a unique number from 1 to 8. The color indicates the dislocation density within the grains. As shown in figure 5(b), grain 2 is rapidly consumed by the neighboring grains 3, 4, and 7. This behavior is expected since grain 2 possesses a higher dislocation density and a smaller size than the surrounding grains, leading to a large combined driving force due to capillarity and stored energy. As microstructure evolution proceeds, grains 3, 4, 5, and 6 are continuously consumed, as shown in figures 5(c) and (d). It is worth noting that the traversed regions that are far away from the initial boundary of the growing grains, such as the left regions of grains 1 and 8, have a nearly uniform deep blue color, implying the reduction of dislocation density to a baseline value. In addition, some of the grain boundaries, such as the one between grains 1 and 8 in

Table 4. Parameters employed in the simulation for microstructure evolution of the confined region. Dimensional values in parentheses denote numerical parameters (not physical parameters).

Parameters	Variable	Value (dimensionless)	Value (dimensional)
Grain boundary energy	γ_{gb}	1.67×10^{-2}	0.595 J m^{-2}
Grain boundary width	l_{gb}	0.1	(4 μm)
Domain size	l	12	4.80×10^2 μm
Grid spacing	$\Delta x = \Delta y$	2.5×10^{-2}	(1 μm)
Bulk energy coefficient	W	1	Not applicable
Gradient energy coefficient	κ	1.25×10^{-3}	Not applicable
Time step	Δt	0.05	Not available

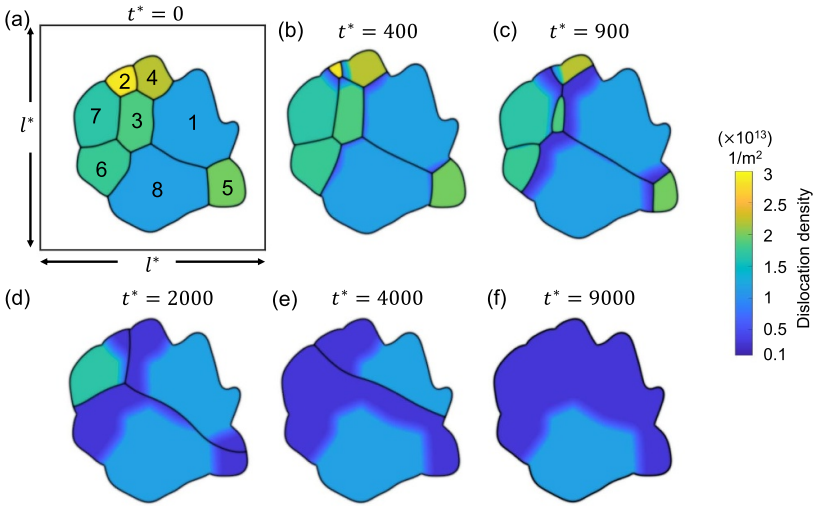

Figure 5. The evolution of microstructure and dislocation density within a confined region found in the experiment (see figure 2). A unique number from 1 to 8 is assigned to each grain. Dislocation densities of all the grains are initialized with equation (16). The color indicates the dislocation density. A black box is plotted in (a) to indicate the simulation domain.

figure 5(d), become curved during microstructure evolution. Such curved boundaries, often associated with island grains or peninsula grains, have been reported in samples that have undergone mechanical deformation and subsequent (isothermal) annealing leading to AGG [57, 58]. The simulation results thus indicate that such curved grains could also be induced by heat treatment alone without mechanical processing. Since grain 8 (with radius $\sim$92 μm) is slightly larger than grain 1 (with radius $\sim$90 μm), the assigned initial dislocation density for grain 8 ($\sim 1.17 \times 10^{13}$ m^{-2}) is lower than that for grain 1 ($\sim 1.19 \times 10^{13}$ m^{-2}). Consequently, grain 8 eventually consumes grain 1, as shown in figures 5(e) and (f), which does not agree with the experimental observation that grain 1 consumes grain 8, as shown in figures 2(c) and (d).

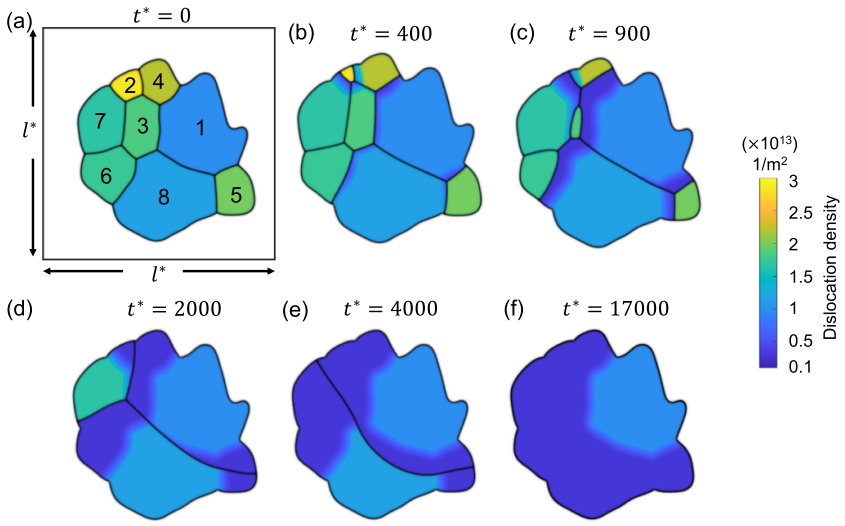

Figure 6. The evolution of microstructure and dislocation density within a confined region found in the experiment (see figure 2). As in figure 5, a unique number from 1 to 8 is assigned to each grain. Dislocation densities of grains 2 through 8 are initialized with equation (16). The dislocation density of grain 1 is reduced by ∼16% from the value given by equation (16), which resulted in a better match with the experimental observation. The color indicates the dislocation density. A black box is plotted in (a) to indicate the simulation domain.

The disagreement could arise from a few potential reasons. First, the simulation is confined to 2D, and the evolution of a cross section within a 3D volume may differ from that of a 2D simulation. Moreover, although the density of the second-phase particles is in general expected to be larger within a smaller grain, there may be statistical variations due to the stochastic nature of precipitate nucleation, growth, and subsequent dissolution that produce dislocations. Finally, it has been known that grain boundary energies are anisotropic, depending on not only the crystalline orientations of the pair of grains but also the relative orientation of the grain boundary plane [59]. The resulting variation in grain boundary energies would result in different probabilities of precipitating second-phase particles on or near grain boundaries, leading to a spread in the density of dislocations produced by the precipitates. Therefore, in reality, the dislocation density within a grain will likely not follow equation (15) exactly, and it is plausible that grain 1 has a lower dislocation density than grain 8. By conducting a parametric sweep, we determined that when the dislocation density of grain 1 is reduced by ∼16% to 10^{13} m^{-2}, grain 1 consumes grain 8 during the simulated evolution. The results of this simulation are shown in figure 6. The early evolution of the two simulations are very similar, as can be seen by comparing figures 5(a)–(c) and 6(a)–(c). On the other hand, during the later stage, grain 1 progressively consumes grain 8, as shown in figures 6(d) and (e), and it is the only grain that remains at the end of the simulation, as shown in figure 6(f). The high dislocation density at grain 1's initial position and the low dislocation density in the surrounding region closely resemble the experimental observations from figure 2(f). Although a quantitative agreement is not expected because of the 2D nature of the simulations and is therefore not a goal of this work, the observed similarities provide support for the proposed model.

Table 5. Parameters employed in the large-scale simulations. Dimensional values in parentheses denote numerical parameters (not physical parameters).

Parameters	Variable	Value (dimensionless)	Value (dimensional)
Grain boundary energy	γ_{gb}	1.46×10^{-2}	0.595 J m^{-2}
Grain boundary width	l_{gb}	8.75×10^{-2}	(3.5 μm)
Domain size	l	69.43	2.78×10^{3} μm
Grid spacing	$\Delta x = \Delta y$	2.19×10^{-2}	(0.876 μm)
Bulk energy coefficient	W	1	Not applicable
Gradient energy coefficient	κ	9.57×10^{-4}	Not applicable
Time step (with stored energy)	Δt_{s}	0.05	Not available
Time step (without stored energy)	Δt_{ns}	0.1	Not available

4.2. Large-scale simulations

In this section, we perform a set of large-scale simulations to examine the effect of CHT on the microstructure evolution. To maintain computational feasibility, the smallest resolvable grain in the simulations is chosen to have a radius of 12 μm. This grain radius requires the interfacial width (defined by order parameter values from $\sim$0.1 to $\sim$0.9) to be no larger than 3.5 μm such that the bulk region within the smallest grain occupies at least 50% of the area, assuming a circular shape of the grain. We initialize the order parameters using the method discussed in sections 3.4.1 and 3.5. The individual dislocation densities are initialized using equation (3). For this equation, the values of $\rho_{0,i}(\boldsymbol{r})$ are given by equation (16) when the dislocations are injected for the first time and by equation (18) when the dislocations are injected for the second and the third times. The values of $\rho_{\text{gb},i}$ are given by equation (17). The dimensionless parameters employed for the simulations are summarized in table 5. Periodic boundary conditions are utilized throughout the simulations.

The initial microstructure, which contains 1778 grains, is shown in figure 7(a). It can be observed from the figure that a number of small grains are clustered in a chain-like structure. This arrangement is reasonable in 2D given the facts that a large portion of small grains was observed in the experiment at state S_1 (see figure 3(a)) and that these small grains would have to cluster in order to avoid an unphysical (non-equiaxed) grain morphology. The high dislocation density of these small grains yields a high stored energy as compared to their surrounding grains, and consequently, these grains are rapidly consumed, as shown in figure 7(b). The microstructure at the end of the first cycle is shown in figure 7(c). Most grains with high dislocation densities (*i.e.* yellow grains) are consumed by their surrounding grains at this stage and the large grains next to these small grains become larger. The corresponding GSDs are shown in figure 8. Note that the probability is scaled to yield an area of unity under the curve. It can be seen that GSD broadens during this cycle (figures 8(a) and (b)), primarily due to the increase in the average grain size. A second cycle is then simulated, which consists of reinjections of dislocations to the microstructure and subsequent microstructure evolution. The increase of dislocation densities is inversely proportional to the grain radius (equation (15)), and therefore the smaller grains experience a higher increase in dislocation densities, as shown in figure 7(d). Microstructures at an intermediate stage and at the end of the second cycle are shown in figures 7(e) and (f), respectively. The GSD continues to broaden, as shown in figure 8(c). A second peak in the GSD appears after the third cycle, as shown in figure 8(d).

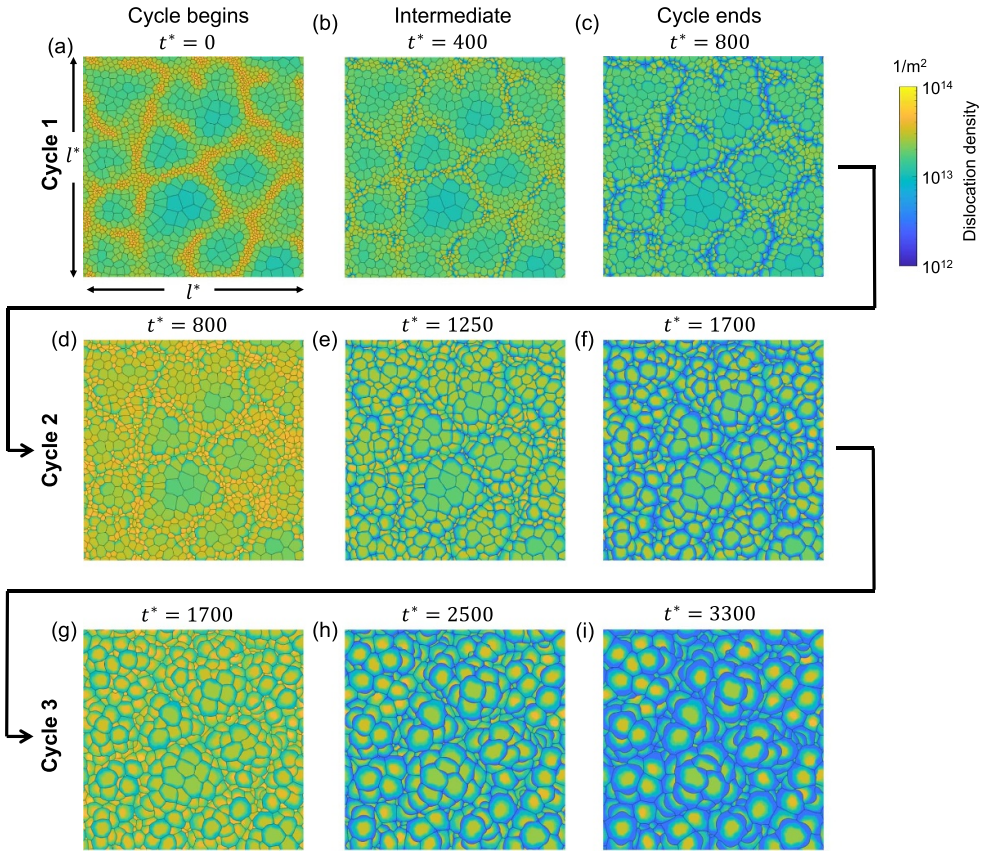

Figure 7. Stored-energy-driven microstructure evolution, after dislocations were injected (a)–(c) once, (d)–(f) twice, and (g)–(i) three times. Each cycle ends when the average grain radius increases by 40%. The dimensionless time t^* is labeled. The color indicates the dislocation density.

The comparison of scaled GSDs for each cycle is provided in figure S4(a) of the supplementary material, in which all the radii are divided by the average radius. The scaled GSD for the simulation with stored energy is clearly not self-similar. Instead, it continues to evolve throughout the three simulation cycles, exhibiting a slight broadening especially at the later cycles, and a bimodal distribution may start to develop at the end of the third cycle. It has been suggested that a bimodal GSD is one of the signatures of AGG [2, 3].

We note that the GSD calculated from the simulated data (figure 8(b)) do not match the experimental result in the S_3 state (see figure 3) on the extreme ends of the distribution. Besides the difference in the dimensionality between the simulation and experiment, there are additional reasons for the discrepancies. On the low end of the radii, the simulation misses some of the smallest grains due to the diffuse interface effect, while the experiment may overestimate the number of small grains due to the noise in the data. On the high end of the radii, the experiment had temperature gradient over the sample, which led to faster grain growth in the hotter end, where the large grains were identified. Furthermore, the timing of the end of the cycle is approximated by the increase in the radius, which introduces additional uncertainty.

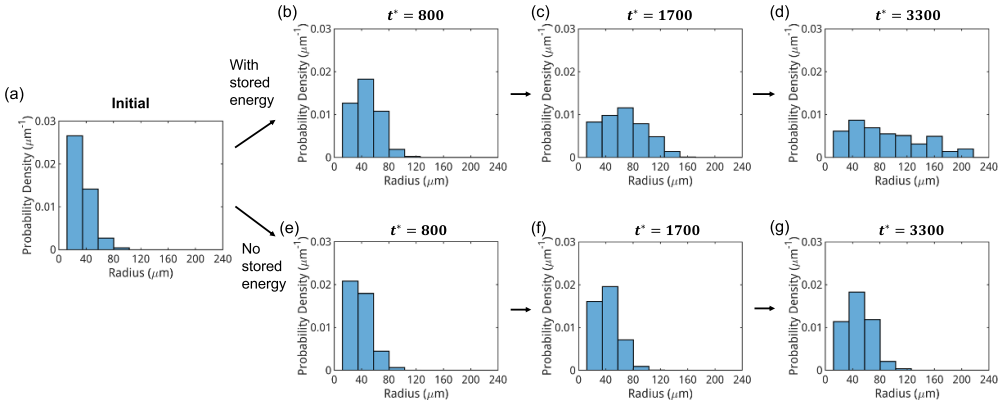

Figure 8. Grain size distributions (GSDs) during the microstructure evolution: (a) at the initial time; (b)–(d) after first, second, and third cycles with stored energy, where $t^* = 800$, $t^* = 1700$, and $t^* = 3300$, respectively, note the cumulative time; and (e)–(g) at $t^* = 800$, $t^* = 1700$, and $t^* = 3300$ for a simulation without stored energy. The probability is scaled to yield an area of unity under the curve.

To confirm that dislocation injections are necessary to yield persistent AGG [60], a simulation that omits the driving force due to the stored energy difference is performed. To allow for a direct comparison, an identical initial microstructure is employed, as depicted in figure 9(a). The microstructure at times $t^* = 800$, 1700, and 3300 during the evolution is shown in figures 9(b)–(d), respectively, which correspond to the final net times of the three cycles for the stored-energy-driven grain growth (*see* figures 7(c), (f), and (i)). In this case, the large grains still progressively consume the smaller grains surrounding them, due to capillarity. To quantify and compare the rate of the microstructure evolution between the simulations with and without the stored energy, we show the average grain radius as a function of time for the two cases in figure 10. The average grain radius during the microstructure evolution with stored energy for cycles 1, 2, and 3 are indicated by red, blue, and black dots, respectively. The average grain radius during the microstructure evolution without stored energy is indicated by green dots. A much faster increase in the average radius is observed when stored energy is considered, which indicates that the microstructure evolution proceeds more rapidly when dislocations are injected *via* CHT. Additionally, at the start of each cycle, there is a rapid increase in the average radius, which is due to the large variation in initial dislocation densities. Then, the growth rate decreases as the stored-energy driving force reduces and the system shifts toward NGG. An additional abrupt increase in the average radius in the middle of cycle 3, observed from time $t^* = 3000$ to 3100, is caused by a significant fraction of grains (14 out of 246 grains) that disappeared between these two times. Unlike the apparent broadening of the GSD observed in the evolution of microstructure with dislocations, the GSD for capillary-driven grain growth only slightly broadens (see figures 8(e)–(g)). In addition, none of the grains are observed to grow abnormally faster than the others. Consequently, the GSD remains singly peaked from $t^* = 800$ to 3300. The convergence to self-similarity is observed in the scaled GSD, as shown in figure S4(b) of the supplementary material.

To further examine the necessity of recurrent dislocation injections to continuously provide stored-energy driving force, we performed an additional simulation in which the dislocations

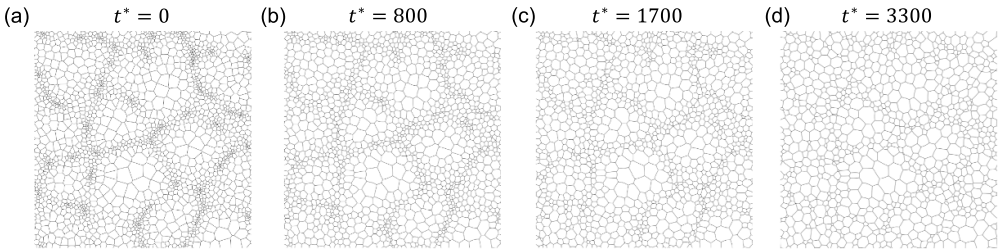

Figure 9. Capillary-driven microstructure evolution, using the same initial microstructure as in figure 7(a). Four snapshots are shown at times (a) $t^* = 0$, (b) $t^* = 800$, (c) $t^* = 1700$, and (d) $t^* = 3300$.

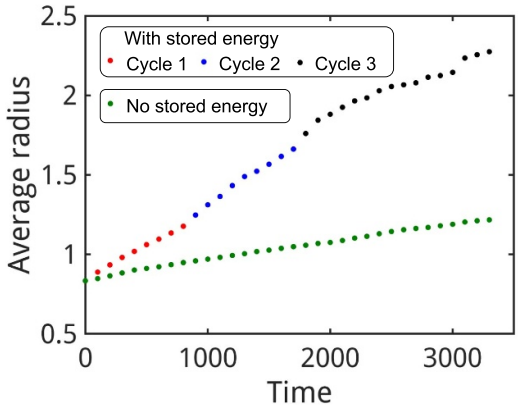

Figure 10. Dimensionless average grain radius *vs*. dimensionless time. The red, blue, and black dots indicate the average grain radius during microstructure evolution with the stored energy contribution for cycles 1, 2, and 3, respectively. The green dots indicate the average grain radius during microstructure evolution without the stored energy contribution.

are only injected once at the beginning. The average grain radius as a function of time from this simulation is shown in figure S3 of the supplementary material, in which red crosses indicate the continued portion, along those of the three-cycle simulation. The microstructure evolution with one-time dislocation injection gradually turns slower, and eventually the rate reduces to a value that is close to that of capillary-driven grain growth, suggesting a progressive transition from stored-energy-driven grain growth to capillary-driven grain growth. In order to prevent such transition, dislocation reinjections are necessary, which provide continuous stored-energy driving force to maintain the rate of microstructure evolution.

5. Conclusions

We developed a PF model for the evolution of microstructure with a spatially varying dislocation density and a reduction in the dislocation density as a grain boundary migrates. We conducted simulations based on the assumption that the smaller grains having higher grain boundary length per unit area (equivalent to surface area per unit volume in 3D) have a higher density of second-phase particles and thus a higher density of dislocations injected. The simulation

predicted a microstructure that closely resembles the experimentally observed microstructure within a region that was confined within a nearly static boundary in the experimental dataset. In addition, the model was utilized to simulate three cycles of stored-energy-driven grain growth within a large microstructure, during which non-self-similar evolution was observed. In contrast, a simulation without the effect of stored energy yielded a near self-similar evolution. In particular, when the stored energy was included assuming that density of dislocations that is injected scales as the inverse of the grain radius (which is expected if the source of dislocations is due to precipitation and dissolution of second-phase particles on or near grain boundaries), it was found not only that grains grew much faster but also the larger grains preferentially grew. Moreover, although the rate of grain growth with stored energy is much faster at the beginning of each cycle as compared to that without stored energy, the former decreases at the later stage of each cycle as the stored-energy driving force reduces with time and the system shifts toward NGG. Therefore, CHT (multiple repetitions of thermal cycling) is necessary to provide an inexhaustible stored-energy driving force.

These simulation results offer a possible mechanism behind persistent AGG during CHT. Additionally, we provided an integrated experimental-computational workflow, which utilizes the information from experiments to inform grain-growth models and its parameterization. While we here limited our efforts to 2D simulations as a proof-of-concept, the workflow can be easily adapted to perform more time-consuming, but more accurate, 3D simulations, as well as to include additional physical considerations, such as recovery. Therefore, our work provides a foundation for future development of simulation tools capable of quantitative predictions of microstructure evolution during non-isothermal heat treatment, which will ultimately facilitate the design of optimized processes for solid-state manufacturing.

Data availability statement

The data that support the findings of this study are openly available at the following URL/DOI: https://doi.org/10.13011/m3-x0qx-yf02.

Code availability

All codes from this study are available from the corresponding author upon reasonable request.

Acknowledgments

This work was supported by the United States National Science Foundation under Award No. DMR-2104786. The computational resources for model development and validation were provided by (1) the National Energy Research Scientific Computing Center, a US Department of Energy Office of Science User Facility located at Lawrence Berkeley National Laboratory, operated under Contract No. DE-AC02-05CH11231 and (2) Stampede2 at the TACC through allocation No. TG-DMR110007 from the Extreme Science and Engineering Discovery Environment, which was supported by National Science Foundation Grant Number #1548562. The computational resource for the large-scale simulations reported in this work was provided by Anvil at the RCAC through allocation No. TG-DMR110007 from the Advanced Cyberinfrastructure Coordination Ecosystem: Services & Support (ACCESS) program, which is supported by National Science Foundation Grants #2138259, #2138286, #2138307, #2137603, and #2138296. The authors would like to thank David Montiel for the

useful discussion. The data presented in this work [61] is published at Materials Commons (materialscommons.org) [62].

CRediT authorship contribution statement

Guanglong Huang: conceptualization, methodology, formal analysis, investigation, writing—original draft, writing—review & editing, visualization. **Alexander Mensah**: methodology, investigation, software, writing—review & editing. **Marcel Chlupsa**: conceptualization, investigation, methodology, formal analysis, writing—original draft, writing—review & editing. **Zachary Croft**: validation, investigation, formal analysis, writing—original draft, writing—review & editing. **Liang Qi:** methodology, writing—review & editing. **Ashwin J. Shahani**: conceptualization, funding acquisition, investigation, project administration, supervision, writing—review & editing. **Katsuyo Thornton:** conceptualization, funding acquisition, investigation, methodology, project administration, resources, supervision, validation, writing—review & editing.

Conflict of interests

The authors declare that they have no known competing financial interests or personal relationships that could have appeared to influence the work reported in this paper.

ORCID iDs

Guanglong Huang https://orcid.org/0000-0002-2627-0901
Alexander Mensah https://orcid.org/0009-0006-9241-4180
Marcel Chlupsa https://orcid.org/0000-0003-2022-2316
Zachary Croft https://orcid.org/0000-0002-6045-4659
Liang Qi https://orcid.org/0000-0002-6038-2907
Ashwin J Shahani https://orcid.org/0000-0002-6157-840X
Katsuyo Thornton https://orcid.org/0000-0002-1227-5293

References

[1] Humphreys F J and Hatherly M 2004 *Recrystallization and Related Annealing Phenomena* ed F J Humphreys and M Hatherly (Elsevier) p 333
[2] Hillert M 1965 *Acta Metall.* **13** 227
[3] Dennis J, Bate P S and Humphreys J F 2007 *Mater. Scie. Forum* **558–559** 717
[4] Furnish T A, Bufford D C, Ren F, Mehta A, Hattar K and Boyce B L 2018 *Scr. Mater.* **143** 15
[5] Zhang J, Shang Y, Liu Q, Wang J, Pei Y, Li S and Gong S 2022 *Crystals* **12** 1017
[6] Park H-K, Han C-H, Park C-S, Park J-T and Joo H-D 2018 *Mater. Charact.* **146** 204
[7] Fang F, Zhang Y X, Lu X, Wang Y, Lan M F, Yuan G, Misra R D K and Wang G D 2018 *Scr. Mater.* **147** 33
[8] Vollmer M, Arold T, Kriegel M J, Klemm V, Degener S, Freudenberger J and Niendorf T 2019 *Nat. Commun.* **10** 2337
[9] Dunn C G and Koh P K 1956 *JOM* **8** 1017
[10] Beck P A and Hu H 1952 *JOM* **4** 83
[11] Kronberg M L and Wilson F H 1949 *JOM* **1** 501
[12] Smith C S 1948 *Trans. Metall. Soc. AIME* **175** 15
[13] Omori T, Kusama T, Kawata S, Ohnuma I, Sutou Y, Araki Y, Ishida K and Kainuma R 2013 *Science* **341** 1500

[14] Kusama T, Omori T, Saito T, Kise S, Tanaka T, Araki Y and Kainuma R 2017 *Nat. Commun.* **8** 354
[15] Omori T, Iwaizako H and Kainuma R 2016 *Mater. Des.* **101** 263
[16] Higgins M J *et al* 2021 *Phys. Rev. Mater.* **5** L070401
[17] Humphreys F J and Hatherly M 2004 *Recrystallization and Related Annealing Phenomena* ed F J Humphreys and M Hatherly (Elsevier) p 215
[18] Koyama T 2008 *Sci. Technol. Adv. Mater.* **9** 013006
[19] Provatas N and Elder K 2010 *Phase-Field Methods in Materials Science and Engineering* (Wiley-VCH) (https://doi.org/10.1002/9783527631520)
[20] Chen L Q 2002 *Annu. Rev. Mater. Res.* **32** 113
[21] Wheeler A A, Boettinger W J and McFadden G B 1992 *Phys. Rev.* A **45** 7424
[22] Kim S G, Kim W T and Suzuki T 1999 *Phys. Rev.* E **60** 7186
[23] Beckermann C, Diepers H J, Steinbach I, Karma A and Tong X 1999 *J. Comput. Phys.* **154** 468
[24] Boettinger W J, Warren J A, Beckermann C and Karma A 2002 *Annu. Rev. Mater. Res.* **32** 163
[25] Gentry S P and Thornton K 2020 *Modelling Simul. Mater. Sci. Eng.* **28** 065002
[26] Takaki T, Yamanaka A and Tomita Y 2015 *From Creep Damage Mechanics to Homogenization Methods: A Liber Amicorum to Celebrate the Birthday of Nobutada Ohno* ed H Altenbach, T Matsuda and D Okumura (Springer International Publishing) p 441
[27] Huang G, Montiel D, McAuliffe R D, Veith G M and Thornton K 2023 *Comput. Mater. Sci* **221** 112080
[28] Gathright W, Jensen M and Lewis D 2011 *Electrochem. Commun.* **13** 520
[29] Bai Y, Mianroodi J R, Ma Y, da Silva A K, Svendsen B and Raabe D 2022 *Acta Mater.* **231** 117899
[30] Chen L Q and Yang W 1994 *Phys. Rev.* B **50** 15752
[31] Fan D and Chen L Q 1997 *Acta Mater.* **45** 611
[32] Krill C E and Chen L Q 2002 *Acta Mater.* **50** 3057
[33] Ko K-J, Cha P-R, Srolovitz D and Hwang N-M 2009 *Acta Mater.* **57** 838
[34] Suwa Y, Saito Y and Onodera H 2007 *Comput. Mater. Sci.* **40** 40
[35] Liu Y, Militzer M and Perez M 2019 *Materials* **12** 4048
[36] Suwa Y and Ushioda K 2022 *ISIJ Int.* **62** 577
[37] Moelans N, Godfrey A, Zhang Y and Juul Jensen D 2013 *Phys. Rev.* B **88** 054103
[38] Bernier J V, Suter R M, Rollett A D and Almer J D 2020 *Annu. Rev. Mater. Res.* **50** 395
[39] Suter R M, Hennessy D, Xiao C and Lienert U 2006 *Rev. Sci. Instrum.* **77** 123905
[40] Li S F and Suter R M 2013 *J. Appl. Crystallogr.* **46** 512
[41] Kang J, Lu N, Loo I, Senabulya N and Shahani A J 2019 *Integr. Mater. Manuf. Innov.* **8** 388
[42] Grabski M W and Korski R 1970 *Phil. Mag.* **22** 707
[43] Piao Y and Le K C 2022 *Contin. Mech. Thermodyn.* **34** 763
[44] Pantleon W 2008 *Scr. Mater.* **58** 994
[45] Williamson G K and Smallman R E 1956 *Phil. Mag.* **1** 34
[46] Moelans N 2011 *Acta Mater.* **59** 1077
[47] Moelans N, Blanpain B and Wollants P 2008 *Phys. Rev.* B **78** 024113
[48] Cahn J W and Hilliard J E 1958 *J. Chem. Phys.* **28** 258
[49] Murr L E 1975 *Interfacial Phenomena in Metals and Alloys* (Addison-Wesley Publishing Company)
[50] Pettersson B 1969 *Phil. Mag.* **20** 831
[51] Cui Y, Chen Z and Ju Y 2019 *Int. J. Solids Struct.* **161** 42
[52] Allen S M and Cahn J W 1979 *Acta Metall.* **27** 1085
[53] Sahagian D L and Proussevitch A A 1998 *J. Volcanol. Geotherm. Res.* **84** 173
[54] Saltikov S A 1967 *Stereology* ed H Elias (Springer) p 163
[55] McKenna I M, Gururajan M P and Voorhees P W 2009 *J. Mater. Sci.* **44** 2206
[56] Permann C J, Tonks M R, Fromm B and Gaston D R 2016 *Comput. Mater. Sci.* **115** 18
[57] Maazi N, Rouag N, Etter A L, Penelle R and Baudin T 2006 *Scr. Mater.* **55** 641
[58] Koo J B, Yoon D Y and Henry M F 2000 *Metall. Mater. Trans.* A **31** 1489
[59] Rohrer G S 2011 *J. Mater. Sci.* **46** 5881
[60] Krill C E, Holm E A, Dake J M, Cohn R, Holíková K and Andorfer F 2023 *Annu. Rev. Mater. Res.* **53** 319
[61] Huang G, Mensah A, Chlupsa M, Croft Z, Qi L, Shahani A J and Thornton K 2004 Phase-field modeling of stored-energy-driven grain growth (Materials Commons) (https://doi.org/10.13011/m3-x0qx-yf02)
[62] Puchala B, Tarcea G, Marquis E A, Hedstrom M, Jagadish H V and Allison J E 2016 *JOM* **68** 2035–44